

## ABSTRACT

Title of Thesis: MODELING ENERGY TRANSPORT IN PORCINE SKIN

Jeff Keslin, Master of Science, 2009

Thesis directed by: Professor Marino di Marzo  
Department of Fire Protection Engineering  
Professor André Marshall  
Department of Fire Protection Engineering

The ability to measure the burn depth in human skin is of great importance in identifying and successfully treating burn injuries. A non-invasive method for measuring this depth is described where a jet of cold air is impinged on the skin and the thermal and physiological response of the skin is observed. A computational model is developed to characterize the temperature response of the dead or burnt skin. This is validated using an experiment involving a jet impinging on a pig skin sample, with temperature measurements made by a non-invasive infrared thermocouple. This data can be used to create and compare a similar model with the inclusion of the physiological response that is present when the test is administered on live or partially burnt skin. Then a correlation may be developed that will predict the burn depth in the affected tissue.

MODELING ENERGY TRANSPORT IN PORCINE SKIN

by

Jeff Keslin

Thesis submitted to the Faculty of the Graduate School  
of the University of Maryland, College Park in partial fulfillment  
of the requirements for the degree of  
Master of Science  
2009

Advisory Committee:

Professor Marino di Marzo  
Professor André Marshall  
Professor Peter Sunderland

## **Acknowledgements**

I would like to extend my gratitude to Dr. Marino di Marzo, Chair of the Fire Protection Engineering department at the University of Maryland for conceptualizing this research and leading it to where it now stands. Also to Dr. André Marshall, Professor of Fire Protection Engineering at the University of Maryland, for his endless support and guidance.

I would also like to thank Dr. James Milke, Professor of Fire Protection Engineering at the University of Maryland, for inspiring me to study fire many years ago. Also, much thanks is owed to my family and friends who have supported me and given me encouragement throughout my entire collegiate career.

## TABLE OF CONTENTS

List of Tables .....	iv
List of Figures .....	v
Chapter I: Introduction and Background .....	1
Current Study .....	3
Chapter II: Experimental Testing .....	4
Experimental Setup .....	4
Testing Results .....	8
Chapter III: Theoretical Model .....	10
Semi-Infinite Solid .....	10
Convective Boundary Condition .....	14
View Angle Adjustment .....	21
Chapter IV: Results .....	25
Model Validation .....	25
Chapter V: Conclusions .....	27
Conclusions .....	27
Future Work .....	28
Appendix A: Tables and Figures .....	30
Appendix B: MATLAB program source code .....	32
References .....	38

## List of Tables

Table 3.1 - Average and local Nusselt numbers as determined by the method in Martin [9] .....	17
Table 3.2 – Local Nusselt numbers for values of $r/D$ ranging from 0 to 3 .....	18
Table A.1 - Input parameters for matching the computational model to the experimental measurements .....	30

## List of Figures

Figure 2.1 - Experimental setup for the application of a cold air jet on a tissue sample ....	5
Figure 2.2 - Diagram of jet and IR thermocouple placement relative to the skin sample below. ....	8
Figure 2.3 – Compiled results from ten successful trials with an internal temperature of 37 °C and a jet temperature of 16 °C. ....	9
Figure 2.4 - Normalized temperature versus time for the pig skin when a jet of 16 °C air is applied.....	10
Figure 3.1 – Diagram showing the nodalization of the test specimen. ....	12
Figure 3.2 - A comparison of the theoretical calculation and the computational model for the temperatures at $t = 200$ seconds .....	14
Figure 3.3 - Average Nusselt number versus radius as determined by Figures 9 and 10 from Martin [9] .....	18
Figure 3.4 - Plot of the Nusselt number versus radius using the two methods within their given ranges of validity .....	19
Figure 3.5 - Plot of the Nusselt number versus radius after adjustment to connect the two calculated sets .....	20
Figure 3.6 - Plot of the normalized jet temperature versus radius that shows the temperature increase as the air cools the surface of the skin and is subjected to mixing with ambient air.....	21
Figure 3.7 - Diagram of the IR thermocouple projection onto the skin surface. When placed at an angle $\theta_v$ , the projection area becomes an ellipse as shown .....	22
Figure 3.8 – Diagram of the view angle correction components.....	23
Figure 4.1 - Comparison of the surface temperatures given by the ADI model and the experimental data .....	27
Figure A.1 – Figures 9 and 10 from [9] that are used to describe the Nusselt number of an impinging jet flow on a flat surface .....	31

## **Chapter I: Introduction and Background**

Exposure to fire and intense heat is a life-threatening situation during the incident and during the subsequent treatment of the injury. According to the American Burn Association [1], there are estimated to be 500,000 treated burn injuries every year in the United States alone. Of these injuries 4,000 result in death. 75 % of these deaths occur at the scene of the incident, whereas the other 25 % occur afterwards or during treatment. Many of these deaths are a result of the difficulty of properly identifying and treating the burn. When the injury is not properly treated a fatal infection can occur. Because of this, it is crucial that a method be developed that can increase the survival rate of such injuries by giving medical professionals a way to better determine the severity and depth of the burn.

In an effort to better understand and predict the temperature response of human skin, Wieczorek and Dembsey [2] developed computational models to describe the skin. The goal was to create a model that could predict pain and 2<sup>nd</sup> degree burns due to a radiant exposure. The study analyzes the effects of epidermal thickness, initial skin temperature, subject age, and other factors on the severity of burn injuries. This resulted in correction factors being applied to simplify the equations for each scenario so that they could be used as efficient burn injury models for engineering purposes.

In a later study [3], Ng and Chua include the presence of the potential for a physiological response in the heat exchange process. A two-dimensional finite element model was produced which was able to predict isotherms within the skin tissue and resulting injury

patterns. In part 2 of their study it was determined that the thermal conductivity of the epidermis and dermis, convective heat transfer coefficient, and initial skin temperature have the most profound influence on the burn injury [4].

Dickey, Holswade, and Lee [5] attempted to measure the resulting burn depth after a heat incident using thermal excitation and imaging. The goal was to utilize a thermal camera to record the skin's response to heating or cooling. A thermal insult would be applied to the skin and the camera would record how the skin returns to its steady state. It was hypothesized that the areas with deeper burns would be further removed from the constant temperature region maintained by the body and would therefore return to its steady-state temperature with a greater relaxation time. The results showed a significant difference in the response of the simulated burn areas and live tissue regions. They concluded that the results were promising, but that further studies needed to be conducted using actual burnt tissue.

Hargroder et al [6] investigated the possibility of measuring the burn depth in human skin using infrared imaging. Analyses were conducted of infrared images taken of hospitalized patients over the course of the first 7 days after the burn incident. They observed the difference in temperature readings between the burn and burn-free regions of tissue. The burnt tissue exhibited temperatures on average 6 °F lower. It was determined that this method has the potential to accurately measure burn depth but that the sample size of this study was too small. Thus, further investigations into the validity of this technique must be made before clinical application.

Sato et al [7] proposed a method of measuring burn depth using photoacoustic signals. This method uses a piezoelectric transducer placed on the skin that measures the acoustic waves originating from the light absorption by the blood. They were able to show that deep burns, deep dermal burns, and healthy tissue, had well differentiated results in laboratory rat specimens. It was concluded that the results also allowed for the quantification of the observed burn depths, but that more testing is needed to test the validity of the method when applied to human skin.

### **Current Study**

This report discusses a recent study conducted at the University of Maryland, College Park. The study uses heat transfer theory and experimental data to create and validate a mathematical model of human skin and its thermophysical reaction to an impinging jet of cold air. This model is designed to replicate fully burnt or dead human skin that is assumed to react like a semi-infinite solid.

The experimental testing for this study was conducted using pig skin, which is known to have similar properties to that of human skin. The pig skin is heated to an internal temperature comparable to the human body and then subjected to an air jet that has been chilled by an ice-water humidifier and flows at a previously prescribed velocity. An infrared thermocouple with a view of where the jet impinges is held above the skin to measure the temperature at its surface.

The goal of these experiments is to validate the theoretical model and to prove that it can accurately describe and predict the temperature response of the skin. The study will compare the results of the experimental testing and the mathematical model and give a better understanding of the skin's behavior. This will become the foundation for the comparison of the temperature reactions of dead and alive skin, and will lead to the analysis that will determine the burn depth within the skin.

## **Chapter II: Experimental Testing**

### **Experimental Setup**

The purpose of this experimental setup is to gain a better understanding of how skin reacts to the application of a concentrated stream of air at a temperature below ambient. This experiment will allow us to validate the theoretical model as well as provide a comparison to the temperature change when the same jet is applied to live skin. The tests were conducted at the University of Maryland's FETS laboratory between May 30, 2008 and June 15, 2008.

The function of the apparatus is to impinge a jet of cold air at approximately 16 °C onto the test specimen. The setup utilizes a humidifier to chill the incoming air and insulated tubing to maintain the sub-ambient temperatures. The air is allowed to flow to the bottom of the humidifier before it is released and forced upward due to its buoyancy. After being chilled inside the humidifier, the air flows to a thin-wall metal tube and released through a nozzle with a diameter of 3 mm. It is released onto the test subject from a distance of 18 mm. The flow and distance are pre-determined by our Nusselt

number calculations, which will be discussed later. A layout of the test setup can be seen in Figure 2.1.

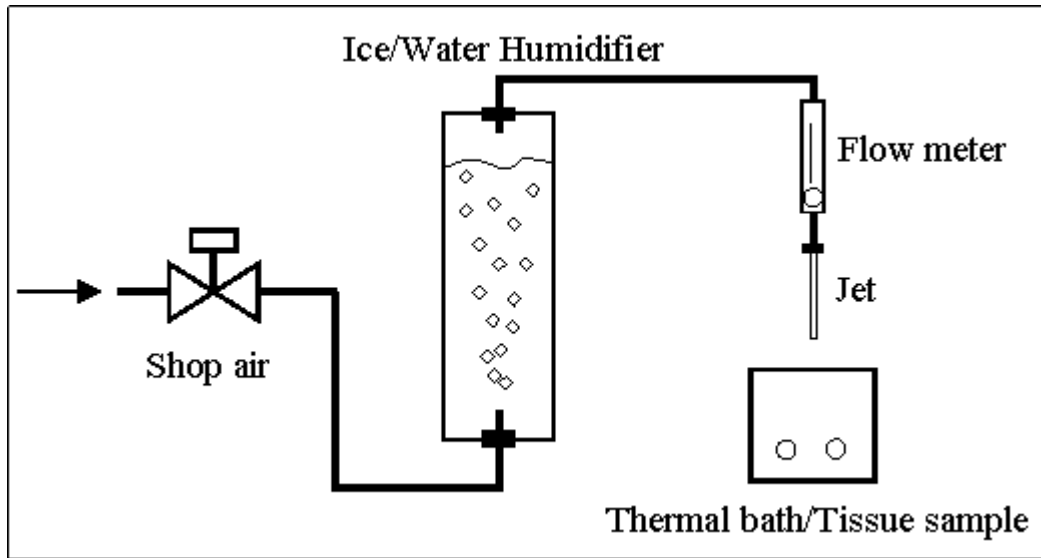


Figure 2.1 - Experimental setup for the application of a cold air jet on a tissue sample

Air was supplied to the testing apparatus by a connection to the FETS laboratory's air supply system. The flow of air was adjusted at the intake by a variable pressure valve. The air was supplied to the system at a pressure of approximately 30 psig. A ¼ inch plastic tube was used to supply the air from the lab to the test setup. A metering valve with a  $C_v$  of 0.04 was then placed in the line in order for the system to be shut on and off, and to allow for the adjustment of the flow so that the proper velocity is obtained at the nozzle.

Once the metering valve is opened, the air travels through another length of plastic tubing into the humidifier. This component chills the air and humidifies it in order to avoid evaporative cooling on the surface of the skin. The humidifier was constructed of 4 inch clear PVC piping with end caps on the top and bottom. The caps were sealed with an

adhesive to ensure that air would not leak from the system. The air enters the humidifier through a drilled hole in the top end cap. Once in the humidifier, the air flows through a thin stainless-steel pipe that extends to the base of the humidifier. In the initial testing it was found that this design did not produce enough heat transfer to chill the air to the desired temperature. The air being released into the humidifier formed large bubbles that minimized the surface area being chilled by the iced water. To improve the heat transfer, plastic tubing was connected to the end of the steel pipe and extended to the bottom of the humidifier. The tubing was then coiled and punctured with small holes on the order of 1 mm. The holes allow for the air to be released into the system in a way that enhances the amount of surface area being thermally affected by the ice water.

Once chilled within the humidifier the air exits through an orifice in the top end cap and to a pressure gauge and flow meter. The meters were used to ensure the proper flow and air velocity through the system. Once the correct flow was obtained, the flow meter was used to observe that the flow was steady and consistent throughout the trials.

Once the proper flow is obtained, the air is sent to the jet, which directs the air onto the test specimen. A thin-walled stainless-steel tubing with an inside diameter of 3 mm was used. The jet and the tubing downstream of the humidifier were insulated with insulating fabric and aluminum foil to allow the air to maintain the sub-ambient temperatures obtained in the humidifier.

The test specimens for these experiments were 4" by 4" swatches of pig skin with approximately 1" of meat still attached underneath the dermis. Pig skin was chosen because of its known similarities to human skin. Since the pig specimen is no longer living, the skin should well represent burnt, or dead, human skin. The temperature at the base of the dermis, or the junction where the skin and the meat connect, was measured by a thermocouple that was inserted into the specimen. The internal temperature was maintained at 37 °C in order to replicate the core temperature of the human body.

The specimen was maintained at 37 °C by a thermal bath. The filling area of the bath is 6" by 6" with a depth of 6". This was an adequate size for the test specimen used in these experiments, which had a surface area of 4" by 4" and a depth of approximately 1". A small stand was placed inside the tank so that the test specimen could rest just above the surface of the water.

The temperature at the impinging point on the surface of the specimen was measured with an infrared thermocouple. The IR thermocouple allows for a temperature reading without invasively affecting the temperature of the specimen. It was placed at a distance of 8 mm from the specimen and at an angle of 45° from the surface. The thermocouple reading results in an average temperature seen over its viewing area. A diagram can be seen in the Figure 2.2.

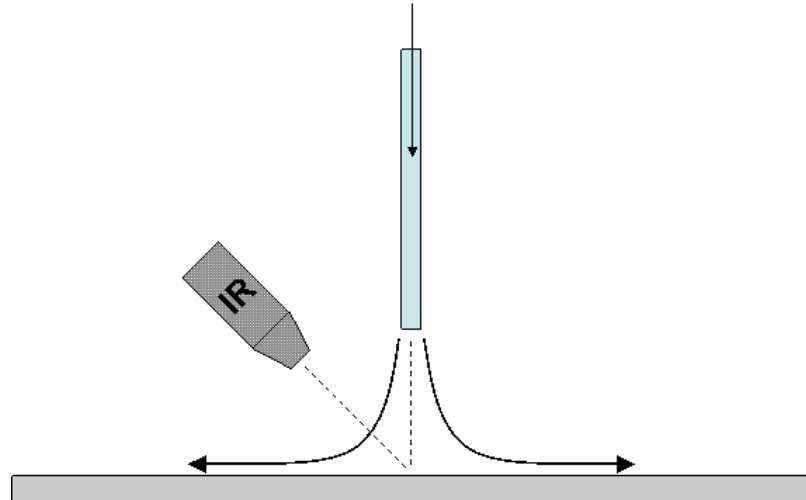


Figure 2.2 - Diagram of jet and IR thermocouple placement relative to the skin sample below.

### Testing Results

Several tests were conducted with the specimen at an internal temperature of 37 °C, and a jet temperature of approximately 16 °C. Before each test these temperatures were given adequate time to reach steady-state conditions. The tests began with the lowering of the jet above the specimen, and the initiation of the IR thermocouple recording device. Data is then collected for 240 seconds, which is enough time for the temperature at the surface to show asymptotic behavior.

Ten successful tests were completed with the data showing adequate precision and repeatability. The measured temperatures,  $T$ , are normalized by the jet temperature and the temperature of the meat-skin boundary. The following equation shows this normalization, where  $\theta$  represents the dimensionless temperature. This results in the data being represented on a scale from 1 to 0.

$$\theta = \frac{T - T_{jet}}{T_{core} - T_{jet}} \quad (2.1)$$

Figure 2.3 shows the data from the successful trials with the measured temperatures normalized. The data shows reasonable agreement between the trials when normalized by the initial temperature as described above. A similar trend in the temperature decay is found for all trials.

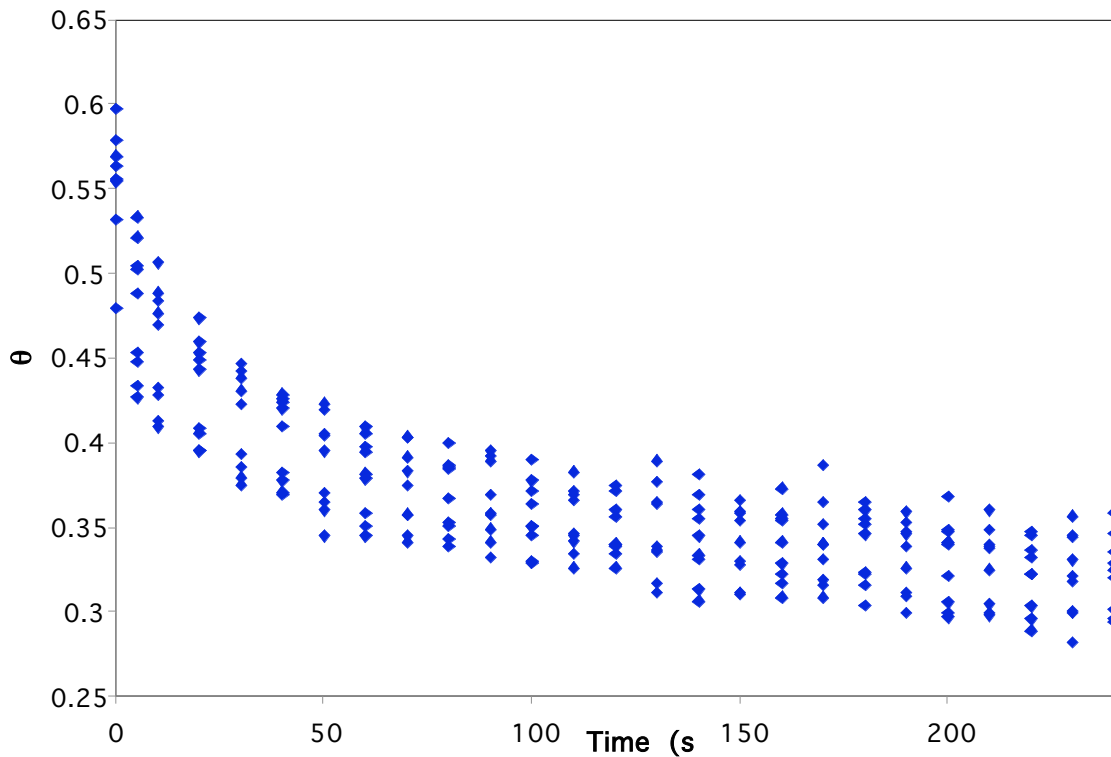


Figure 2.3 – Compiled results from ten successful trials with an internal temperature of 37 °C and a jet temperature of 16 °C.

The following plot shows the average value at each time step given by the data with corresponding error bars that represent one standard deviation from the mean.

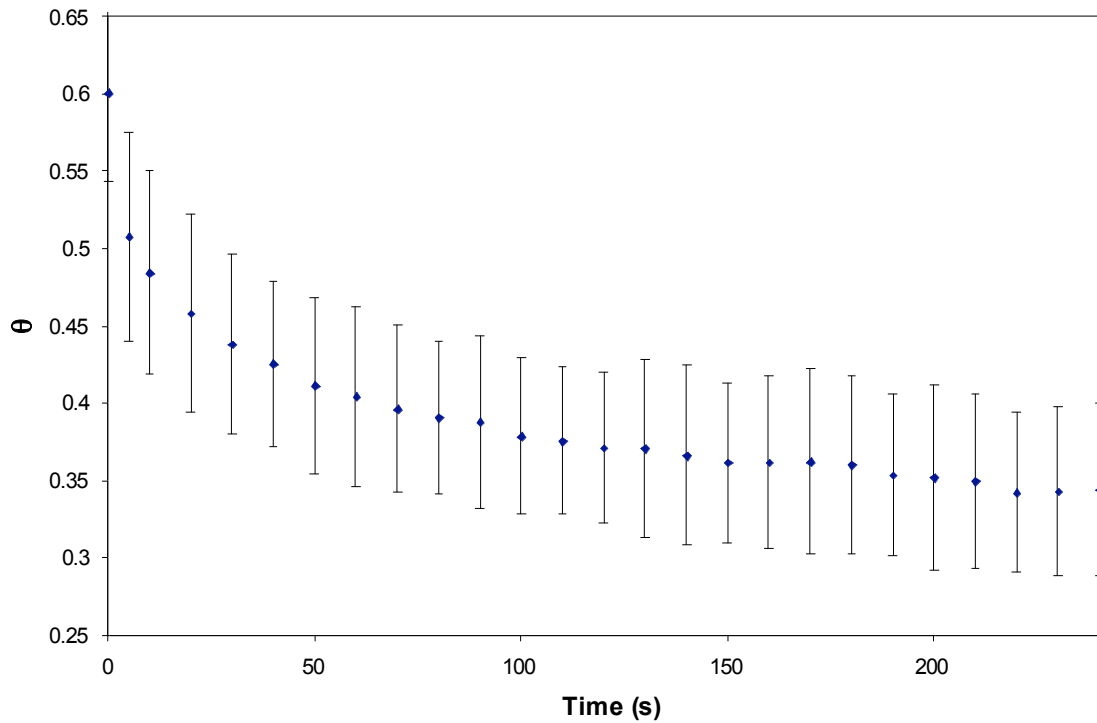


Figure 2.4 - Normalized temperature versus time for the pig skin when a jet of 16 °C air is applied

The plot shows the exponential decay expected from the theoretical equations. Typically temperatures would begin at approximately 28 °C and reach steady state around 22 °C.

This results in an average temperature drop of 6 °C. This is an adequate temperature range that will serve as the comparison and validation of the computer model.

### Chapter III: Theoretical Model

#### Semi-Infinite Solid

The skin specimen examined in the experimental testing can be treated like a semi-infinite solid for modeling purposes. The governing equation used for this scenario is an

expression of Fourier's Law for heat diffusion. Cylindrical coordinates are used here because of the radial nature of the impacting jet on the skin. For these experiments,

$$\frac{\partial T}{\partial t} = \frac{k}{\rho c} \left[ \frac{\partial^2 T}{\partial r^2} + \frac{\partial^2 T}{\partial z^2} + \frac{1}{r} \frac{\partial T}{\partial r} \right] \quad (3.1)$$

where;

$$\text{at } r = \text{large}, T = T_{0,skin}$$

$$\text{at } z = 3\text{mm}, T = 37^\circ\text{C}$$

$$\text{at } z = 0, h(T_\infty - T_s) = -k \frac{dT}{dz}$$

$$\text{at } r = 0, \frac{\partial T}{\partial r} = 0$$

$$\text{at } t = 0, T = T_{0,skin}$$

In order to create a computational model that will accurately describe the temperatures at the surface of the test specimen, a nodalization of the test sample was created. The nodalization allows for the computation of temperatures at precise points along the radial dimension of the skin and the depth. The distance between each point of interest, or node, along the r axis is  $\Delta r$ , and the distance between nodes in the z direction is  $\Delta z$ . For simplicity,  $\Delta r = \Delta z$  throughout the computation. The origin was chosen to be the point directly below the nozzle where the jet impacts the skin. This can be seen in Figure 3.1.

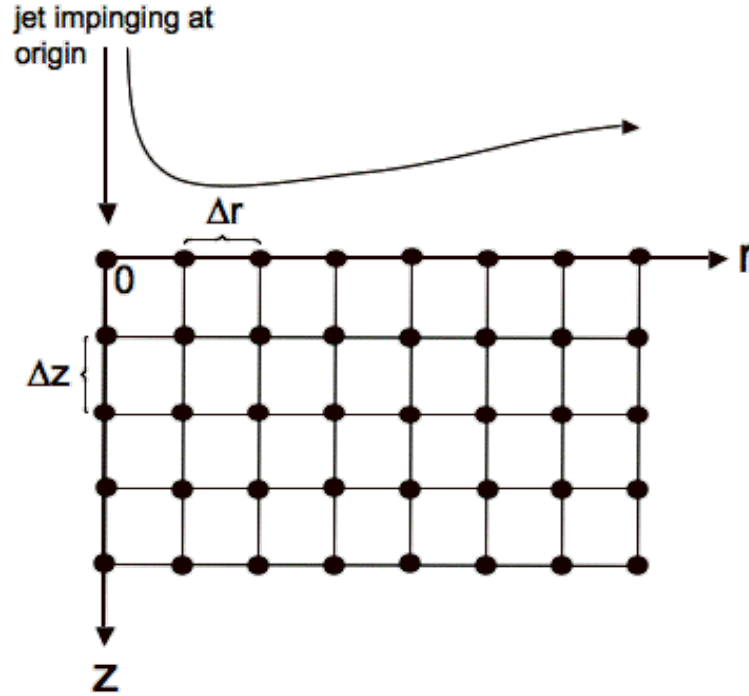


Figure 3.1 – Diagram showing the nodalization of the test specimen.

Now that a 2-dimensional grid of nodes has been determined, a method of temperature calculation must be chosen. The alternating-direction implicit (ADI) method was used to obtain a finite-difference form of the heat diffusion equation above. This allows for the stability of using an implicit scheme, while also enabling the use of tridiagonal matrices, which drastically reduces calculation time. In this scheme, each time increment is done in two half steps. The discretized version of the heat equation above using the ADI method is as follows.

$$\frac{T_{i,j}^{l+1/2} - T_{i,j}^l}{\Delta t/2} = \frac{k}{\rho c} \left[ \frac{T_{i,j+1}^l - 2T_{i,j}^l + T_{i,j-1}^l}{(\Delta z)^2} + \frac{\left(1 + \frac{1}{2(i+1)}\right)T_{i+1,j}^{l+1/2} - 2T_{i,j}^{l+1/2} + \left(1 - \frac{1}{2(i-1)}\right)T_{i-1,j}^{l+1/2}}{(\Delta r)^2} \right] \quad (3.2)$$

$$\frac{T_{i,j}^{l+1/2} - T_{i,j}^l}{\Delta t/2} = \frac{k}{\rho c} \left[ \frac{\left(1 + \frac{1}{2(i+1)}\right) T_{i+1,j}^l - 2T_{i,j}^l + \left(1 - \frac{1}{2(i-1)}\right) T_{i-1,j}^l}{(\Delta r)^2} + \frac{T_{i,j+1}^{l+1/2} - 2T_{i,j}^{l+1/2} + T_{i,j-1}^{l+1/2}}{(\Delta z)^2} \right] \quad (3.3)$$

To validate a simplified version of the model, the sample is treated like a uniform temperature semi-infinite solid with constant temperature boundary conditions. The boundary that represents the surface of the skin is set to 0 °C and the temperature of the solid is initially at 100 °C. It is assumed that this array of temperatures at  $r=0$  would be approximately equal to the array of temperatures given by the theoretical computation of a 1-dimensional thermal conduction problem. The resulting temperature of the centerline at 200 seconds can then be compared to the values given by the 1-dimensional solution for this scenario of a constant surface temperature. Solving the following equation for  $T(x,t)$  allows for the temperature distribution through the thickness of the skin [8].

$$\frac{T(x,t) - T_s}{T_i - T_s} = \operatorname{erf}\left(\frac{x}{2\sqrt{ct}}\right) \quad (3.4)$$

where;

$$\begin{aligned} T_s &= 0 \text{ } ^\circ\text{C} \\ T_i &= 100 \text{ } ^\circ\text{C} \end{aligned}$$

Figure 3.2 shows the temperature of the node versus its distance from the surface of the skin. The theoretical calculation and the cylindrical model show precise agreement well within 1 %. This demonstrates that the model is recreating the conduction through the skin accurately, and now it is ready for the addition of the more complicated convective boundary condition.

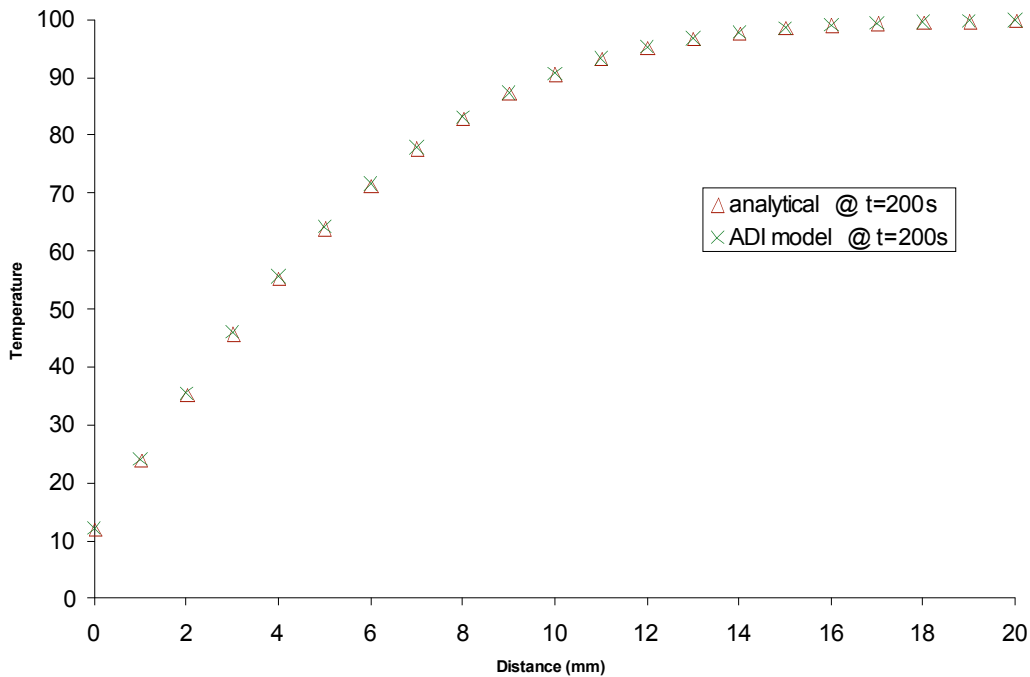


Figure 3.2 - A comparison of the theoretical calculation and the computational model for the temperatures at  $t = 200$  seconds

### Convective Boundary Condition

The surface of the test specimen will be impacted by the flow of cold air from a circular jet. The air will then continue radially outward from the center of the jet impact position. Because the velocity and the temperature of the air will vary depending on its distance from the point of impingement, the problem of the convective boundary condition becomes complicated. In order to properly represent the velocity of the air at each surface node, the Nusselt number for the flow must be calculated as a function of the radial distance from the point of impingement.

The following equation expresses the average Nusselt number as a function of  $r$  and Reynolds number [8]. This correlation has a range of validity from an  $r/D$  of 2.5 to 7.5.

$$\frac{\bar{Nu}_D}{Pr^{.42}} = \frac{D}{r} \left[ \frac{1 - 1.1(D/r)}{1 + 1.1(H/D - 6)(D/r)} \right] \cdot f(Re) \quad (3.5)$$

where;

$$\begin{aligned} f &= 2 Re^{1/2} (1 + 0.005 Re^{0.55})^{1/2} \\ Pr &= .707 \\ D &= .003 m \end{aligned}$$

Here,  $H$  is the height of the jet above the specimen surface and  $D$  is the jet diameter. For this study the jet was placed at 18 mm so that the  $H/D$  value would equal 6, making the term in the denominator equal to 1, and thus simplifying the equation to:

$$\frac{\bar{Nu}_D}{Pr^{.42}} = \frac{D}{r} [1 - 1.1(D/r)] \cdot f(Re) \quad (3.6)$$

In order to find the local Nusselt number from  $\bar{Nu}$ , the following relationship is used.

$$\bar{b} = \frac{2}{r^2} \int_0^r b(r') r' dr' \quad (3.7)$$

where;

$$b = \frac{Nu_D}{Pr^{.42}}$$

By taking the derivative,  $b$  can be determined in terms of  $\bar{b}$ :

$$\frac{\partial}{\partial r} \left( \frac{r^2 \bar{b}}{2} \right) = \frac{\partial}{\partial r} \int b(r') r' dr' \quad (3.8)$$

Therefore;

$$b = \bar{b} + \frac{r}{2} \frac{\partial \bar{b}}{\partial r} \quad (3.9)$$

By inserting Equation (3.5) into the resulting equation for  $b$ , the local Nusselt number for this range is determined to be:

$$\frac{Nu_D}{Pr^{0.42}} = \left[ \frac{D}{2r} \right] \cdot f(Re) \quad (3.10)$$

For this study a  $Re$  of 2000 was chosen, therefore  $f = 103$ . This simplifies Equation (3.9) to:

$$Nu_D = \frac{0.139}{r} \quad (3.11)$$

where  $r$  is in  $mm$ .

Because of the previously defined range of this function, it will be used for an  $r/D$  of 2.5 to 7.5. In order to define the local Nusselt numbers for  $r/D$  values that are less than 2.5, the experimental data found in Martin [9] will be used. For this analysis, the Nusselt number will be expressed as shown before as:

$$Nu_D = \bar{Nu} + \frac{r}{2} \frac{\partial \bar{Nu}}{\partial r} \quad (3.12)$$

Martin shows the average Nusselt number as a function of Reynolds number. The values from Table 3.1 were determined from Figures 9 and 10 from [9]. This is valid for an  $r/D$  of up to 3.

Table 3.1 – Average Nusselt numbers as determined by figures in [9]

$r/D$	$r$ (mm)	$Nu/Pr^{0.42}$	Correction	$Nu_{(avg)}$
0	0	50	1.03	44
1	3	40	1.04	36
2	6	28	1.06	26
3	9	22	1.06	20

Using this data, the change in average Nusselt number by the change in  $r$  can be determined by finding the slope of the following plot, Figure 3.3. The plot shows there is a linear relationship between the average Nusselt number and the radius for this range of data. The value of the derivative of the average heat transfer coefficient with respect to  $r$  will therefore be, -2.733. Now the local Nusselt number,  $Nu_D$ , can be calculated. This is shown in Table 3.2.

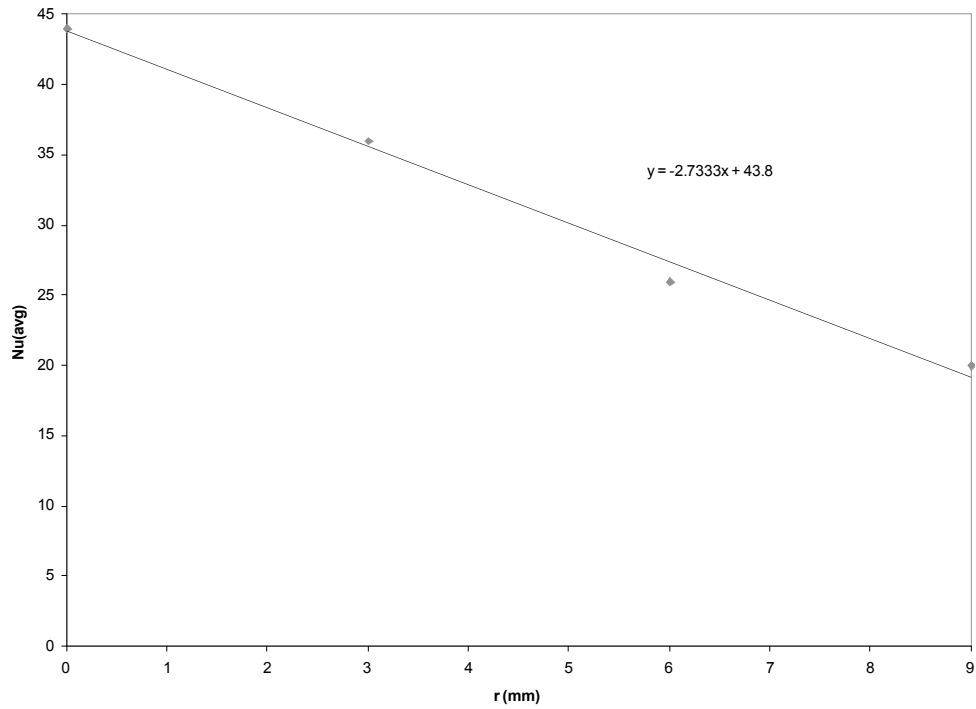


Figure 3.3 - Average Nusselt number versus radius as determined by Figures 9 and 10 from Martin [9]

Table 3.2 – Local Nusselt numbers for values of  $r/D$  ranging from 0 to 3

$r/D$	Nu
0	34
1	22
2	18
3	15

Now there are local Nusselt numbers to describe the flow at all radial locations from the impingement point of the jet. The following plot shows the values determined by the two methods over their given ranges.

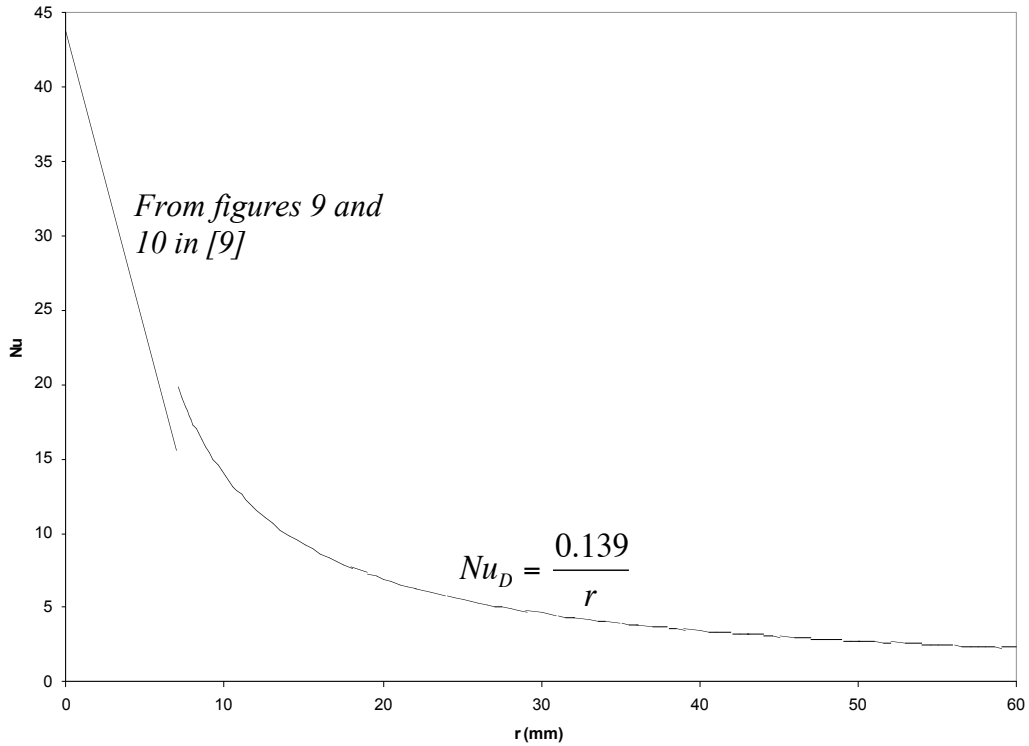


Figure 3.4 - Plot of the Nusselt number versus radius using the two methods within their given ranges of validity

It can be seen there is a discontinuity in the area where the two methods reach their limits of validity. In order to produce an applicable curve, the region where the two functions are discontinuous was adjusted to make one coherent set of values. The figure below shows the Nusselt number as a function of distance from the point of impingement for this flow scenario with the necessary adjustments made.

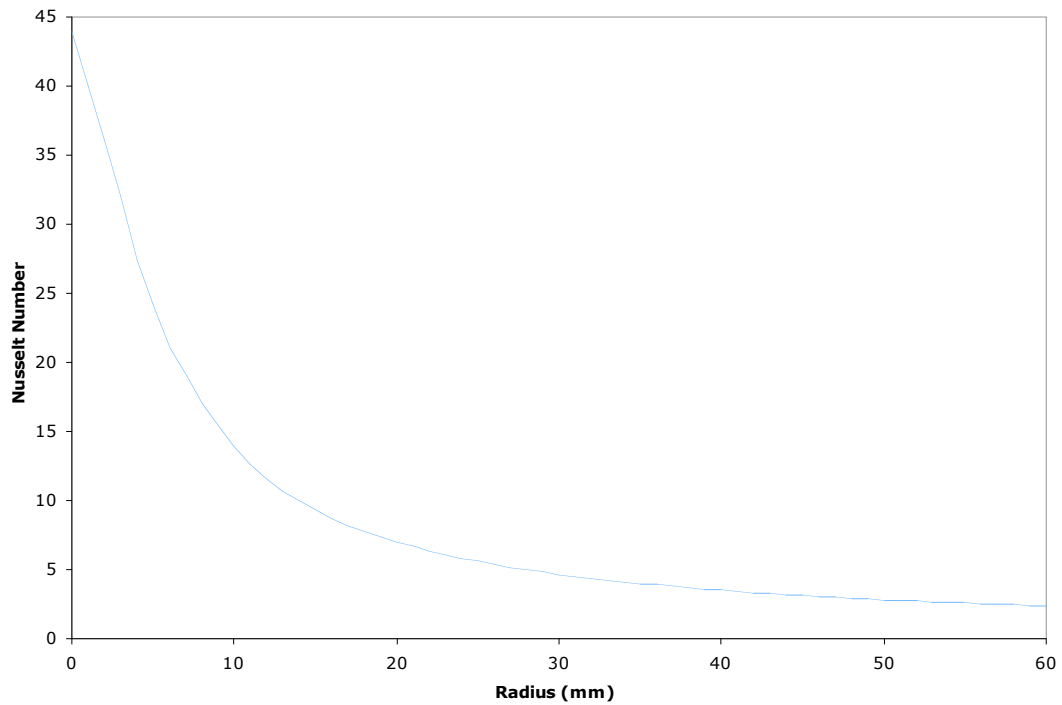


Figure 3.5 - Plot of the Nusselt number versus radius after adjustment to connect the two calculated sets

The temperature of the air released from the jet will also be a function of the radial distance from the point of impingement. Once the air is released from the nozzle it will be subject to mixing with the ambient air. It will also be gaining energy as it cools the surface of the skin. Because of the difficulty of measuring this delicate change, assumptions have been made about the temperature response of the air. The air is assumed to reach the ambient temperature by the time it flows from the point of impingement to a radius of 60 mm. It is also assumed that the growth is exponential, and the jet temperature,  $T_{jet}$ , can be expressed as seen below.

$$T_{jet} = T_{\infty} \left( 1 - \left( 1 - \frac{T_{jet,in}}{T_{\infty}} \right) e^{-A \cdot r} \right) \quad (3.13)$$

$T_{jet,in}$  is the initial temperature measured at the nozzle, and  $A$  is a constant arbitrarily chosen to give a reasonable curve. The figure shows the temperature of the jet as a function of radius normalized by the ambient and initial jet temperatures. For this model,  $A$  was chosen to be  $.077 \text{ mm}^{-1}$ .

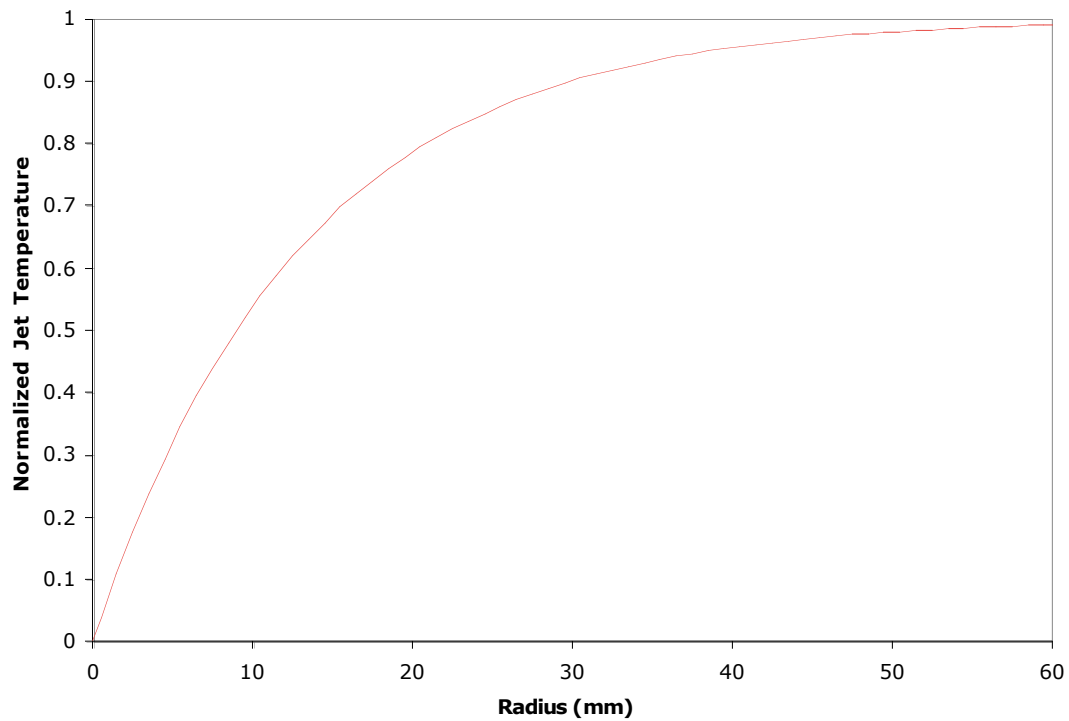


Figure 3.6 - Plot of the normalized jet temperature versus radius that shows the temperature increase as the air cools the surface of the skin and is subjected to mixing with ambient air.

### View Angle Adjustment

The temperature of interest in this study is the surface of the skin specimen. This temperature is measured by an infrared thermocouple. The thermocouple is placed above

the skin but not directly over the point of impingement because it must avoid contact with the jet. This means that in order to measure the temperatures at the center, the IR thermocouple must be placed to the side of the nozzle and at an angle. Because of the viewing angle of the thermocouple, what would normally be a circular viewing region now becomes an ellipse, as shown in Figure 3.7. This must be accounted for in the modeling results. In order to do so the following method of viewing angle adjustment was applied.

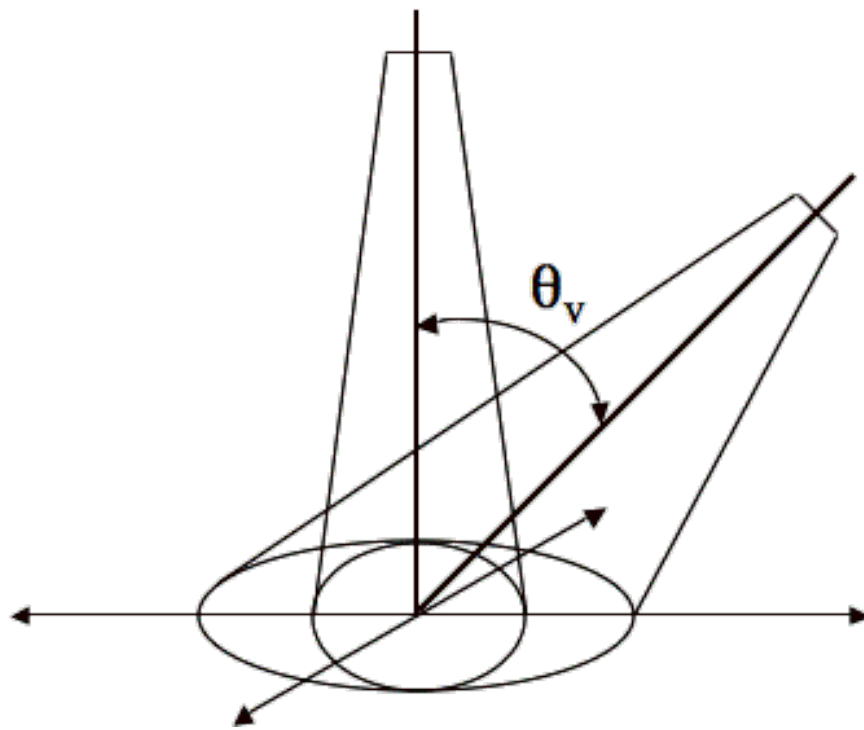


Figure 3.7 - Diagram of the IR thermocouple projection onto the skin surface. When placed at an angle  $\theta_v$ , the projection area becomes an ellipse as shown

In order to properly describe the surface area being viewed by the angled thermocouple, the area where the ellipse extends beyond the circle that exists when  $\theta_v = 0^\circ$  must be accounted for. To achieve this, the nodes that extend beyond the inner circle (which has a radius,  $R$ ) will be multiplied by some factor,  $F$ , which describes the fraction of the

radial area from that point that is included in the ellipse. For the following analysis,  $n_1$  is considered the number of surface nodes inside the circle described by  $\theta_v = 0^\circ$ , and  $n_2$  is the number of surface nodes within the area of the ellipse when  $\theta_v = 45^\circ$ . Figure 3.8 shows the angle of interest,  $\theta_F$ , where the ellipse and radial distance for node  $n$  intersect.

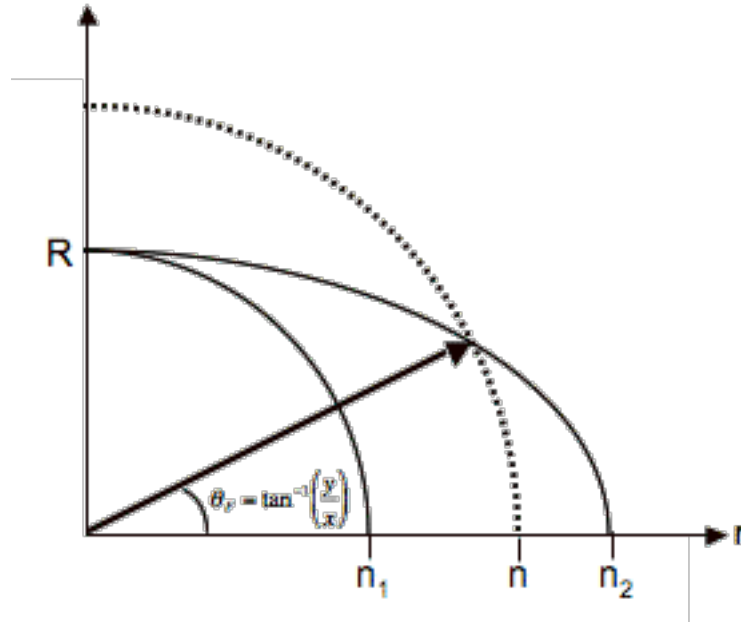


Figure 3.8 – Diagram of the view angle correction components

To find the intersection shown in the figure above, the equations for the circle and the ellipse can be made equivalent. The equations for a circle and an ellipse can be expressed as,  $x^2 + y^2 = R^2 \epsilon^2$  and  $x^2 \cos^2 \theta + y^2 = R^2$ , where  $\epsilon$  is the eccentricity and has a range of 1 to  $\frac{1}{\cos(\theta)}$ . In this experimental setup, the viewing angle was set to  $45^\circ$ . By

solving the ellipse equation for  $y^2$  and substituting:

$$x^2 = \frac{R^2(\epsilon^2 - 1)}{\frac{1}{2}} \quad (3.14)$$

$$y^2 = R^2(2 - \varepsilon^2) \quad (3.15)$$

Therefore, the angle of interest,  $\theta_F$ , that describes the intersection of the circle and the

ellipse can be determined by finding the arctangent of  $\frac{y}{x}$ :

$$\theta_F = \tan^{-1}\left(\frac{y}{x}\right) \quad (3.16)$$

$$\theta_F = \tan^{-1}\left(\sqrt{\frac{2 - \varepsilon^2}{2\varepsilon^2 - 2}}\right) \quad (3.17)$$

The angle,  $\theta_F$ , is now the angle from the origin. By dividing this value by  $90^\circ$ , or  $\frac{\pi}{2}$ , the

fraction of the circular area inside the ellipse,  $F$ , is determined:

$$F = \frac{2\theta_F}{\pi} \quad (3.18)$$

The average temperature,  $\bar{T}$ , as seen by the IR thermocouple can now be expressed as:

$$\bar{T} = \frac{T_1}{n_1^2 \sqrt{2}} + \frac{2}{n_1^2 \sqrt{2}} \sum_2^{n_1} (n - \frac{1}{2}) T_n + \frac{2}{n_1^2 \sqrt{2}} \sum_{m_1+1}^{n_2} (n - \frac{1}{2}) T_n \cdot F \quad (3.19)$$

where;

$n$  = number of nodes from the center

$n_1$  = number of nodes to the edge of the original circle

$n_2$  = number of nodes to the tip of the ellipse area

$T_n$  = Temperature of the node

$$\varepsilon = \frac{n - 0.5}{n_1}$$

This average temperature will be used in the computer model as the comparison to the temperature values given in the experimental data.

## Chapter IV: Results

### Model Validation

The goal of this study is to gain a better understanding of the thermal response in skin tissue when acted on by an impinging jet. In order to gain this understanding, a computational model was created that predicts the skin's response to a cold jet in the absence of physiological interference. An experimental setup was developed to form data that could validate the model. The results of the experimental data and the theoretical model are compared to determine the accuracy of the model.

The computational model, written in the MATLAB<sup>®</sup> computing language, utilizes the alternate-direction implicit (ADI) method of finite-difference calculation. Thus the computation is both convergent and stable regardless of the values chosen for  $\Delta r$  and  $\Delta t$ . This method also results in the use of tridiagonal matrices, which enhance the simplicity of the model and decrease computation time. In order to better represent the circular nature of the jet, the ADI was converted from Cartesian, to cylindrical coordinates with  $r = 0$  placed at the central point of the impact of the jet. This results in a two-dimensional representation of the skin with  $z$  representing the depth and  $r$  representing the radial distance from the center of the specimen.

Table A.1 shows the input parameters used in the computer model. The model was written such that  $\Delta z$  and  $\Delta r$  must be equal for the equations to hold true. For this scenario, a  $\Delta r$  of 0.25 mm was chosen so that the model will have an adequate amount of data points in each coordinate direction. To avoid the additional complications of the

heat transfer in the meat below the dermis, the constant temperature boundary is set at 3 mm from the surface of the skin. This is the depth where the dermis and the meat are connected. This results in there being 12 nodes in the z-direction. It was determined that 35 mm was an adequate radial distance from the center to assume a constant temperature boundary. This allows for 140 nodes in the r-direction. The thermal conductivity was chosen to be 0.21 W/mK as determined in a similar study by [10]. The thermal conductivity of the air was given as 0.026 W/mK for this range of temperatures [8]. The initial temperature of the skin surface, temperature of the jet, and temperature of the skin-meat interface were chosen to correspond with the values found in the experimental setup. The initial temperatures through the depth of the skin are assumed to follow a linear increase from the surface temperature to the constant temperature at the 3 mm depth of the dermis.

The model was used to calculate the temperatures of the skin along its surface and throughout its depth. The temperatures at the surface, however, are the temperatures of interest for this study. Using the surface temperatures given by the model, the temperatures as seen by the IR thermocouple were calculated using the view angle correction discussed previously. This results in one average temperature for each time step of 1 second. The results of the model can be seen in Figure 4.1. The temperatures were normalized by the core and jet temperatures in order to create a set of data points from 1 to 0. The trend produced by the computation closely resembles that of the experimental data. At each data point, the curve created by the model lies within one standard deviation of the mean. The curve shows especially close agreement between the

10 and 60 second marks. The average final temperature observed at 240 seconds in the experiments was 22.5 °C. The final temperature calculated by the model was 22.1 °C. This is a discrepancy of approximately 2 %. This shows that the model can accurately simulate the effects of an impinging jet on the temperatures of a skin sample when physiological responses are not present.

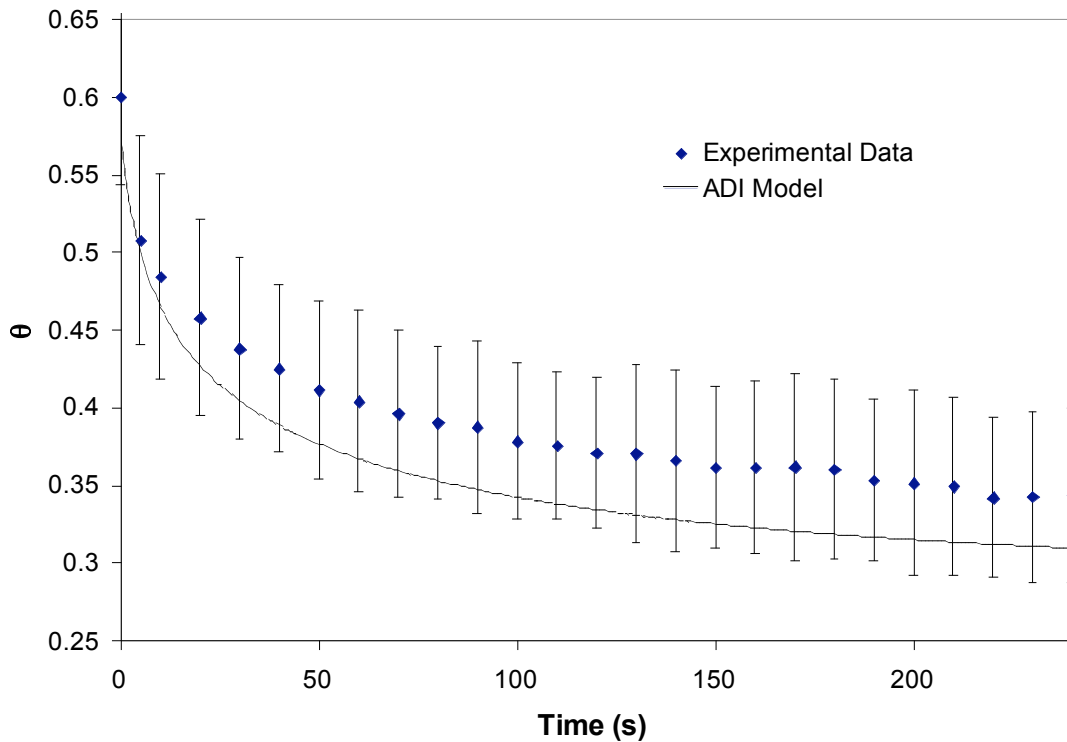


Figure 4.1 - Comparison of the surface temperatures given by the ADI model and the experimental data

## Chapter V: Conclusions

### Conclusions

This study provided further knowledge and understanding of how skin reacts thermally to a cooling jet. A model was created to simulate this effect and was validated using an experimental setup involving pig skin. The model was able to accurately reproduce the

trends found in the data. This testing represents the application of the jet to a skin sample with no physiological response affecting the heat exchange. This is expected to represent the thermal response of severely burnt or dead skin. This model will be used in further studies as a comparison to the thermal response of live or partially burnt skin. The model has proven to be an effective baseline for the studies that will lead to a method of determining burn depth in human skin using thermal response measurements.

### **Future Work**

The model developed in this study is the foundation of the analysis that can lead to the non-invasive measurement of the burn depth in human skin. The computer model properly represents the thermal response of a fully burnt or dead skin sample. This can be used as a comparison to the response of live or partially burnt skin.

In order to compare these physiologically dissimilar responses, testing will have to be done on live human tissue. A similar test setup can be used to measure the temperatures of the sample. However, it may be necessary to use a different method of air cooling in order to obtain lower temperature values than the ones used in this study. It is expected that it will take a more severe sub-ambient temperature to excite an anatomical response that will affect the temperature results.

Once this data is obtained, analysis can be conducted involving the two dissimilar responses. In order to simplify and improve the accuracy of the analysis, a dimensionless time should be used in the calculation and visualization of the data. This will eliminate

the difficulty in addressing the difference in thermal properties between subjects. Then, testing in cooperation with a medical institution involving test subjects with burn injuries can lead to a correlation that will describe the relationship between the temperature curve and the burn depth in the skin.

## Appendix A: Tables and Figures

Table A.1 - Input parameters for matching the computational model to the experimental measurements

<b>Input</b>	<b>Value</b>	<b>Units</b>
$\Delta r$	0.25	mm
Nodes in r-direction	140	
Nodes in z-direction	12	
$k_{\text{skin}}$	0.21	W/mK
Skin $cp*\rho$	4186800	J/m <sup>3</sup> K
$k_{\text{air}}$	0.026	W/mK
Initial jet temp	16	°C
Ambient air temp	19	°C
Initial surface temp	28	°C
Skin thickness	3	mm
Skin temp @ 3 mm	37	°C

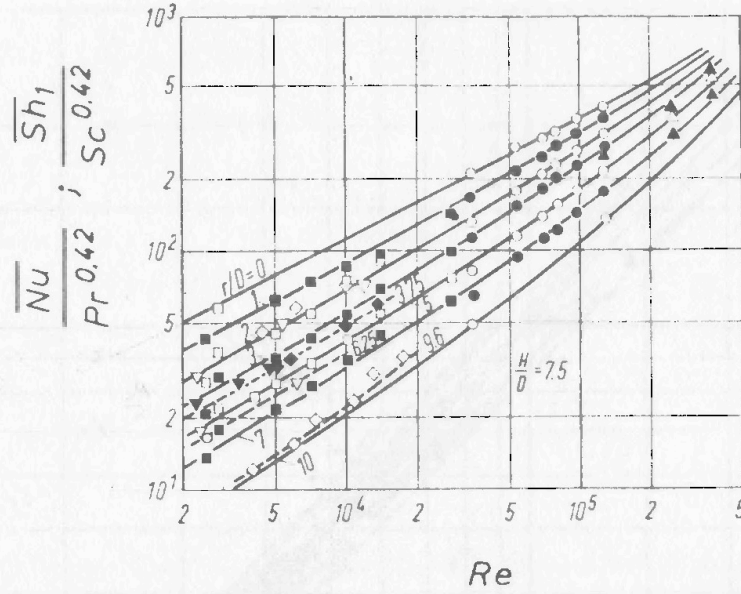


FIG. 9. Heat and mass transfer for impinging flow from single round nozzles at  $H/D = 7.5$  [1]. ●○ Schlünder and Gnielinski; ▲△ Petzold; ■□ Gardon and Cobonpue; ▼▽ Brdlick and Savin ( $r/D = 2.34, 3.75, 6.25$ ); ◆◇ Smirnov *et al.* ( $r/D = 2.24, 3.75, 9.6$ ).

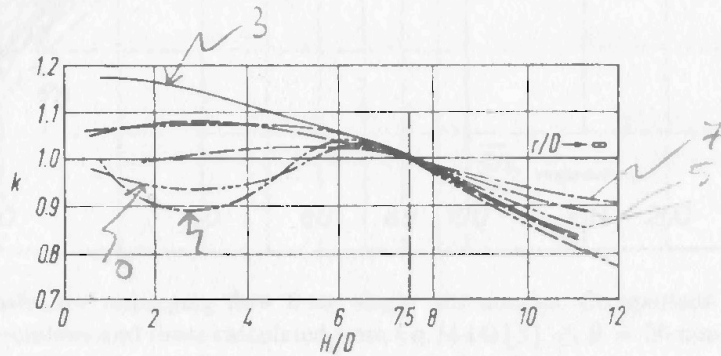


FIG. 10. Correction function  $K(H/D, r/D)$  to Fig. 9 for relative nozzle-to-plate distances  $H/D$  other than 7.5 [1].  $r/D$ : ····· 0, ····· 1, ····· 2, ····· 3, ····· 5, ····· 7.

Figure A.1 – Figures 9 and 10 from [9] that are used to describe the Nusselt number of an impinging jet flow on a flat surface

## Appendix B: MATLAB program source code

### Program 1: Cylindrical Semi-Infinite Solid with Constant Temperature Boundary

```
%Transient heat transfer for semi-infinite solid with an initial temp
of Ti,
%with an upper boundary of convective heat transfer where Tj < Ti.
%Load workspace: ADInxmconv.mat
%n = grid dimension representing the number of rows in the boundary
layer
n=10;
%m = grid dimension representing the number of columns in boundary
layer
%Note: m must be an odd integer
m=10;
dx=.001;
%Define initial grid temperatures
T = [];
%Ti = temperature of the specimen @ t=0
Ti = 1;
T = Ti*ones((n+2),(m+2));
%Define Jet properties
Tj=.5; kair=.025; D=.003;
Nuint = spline(X,Nu,.5*dx:dx:.06-.5*dx);
Xint = (.5*dx:dx:.06-.5*dx);
T(1,:) = Tj;
%Define heat transfer and grid properties
k=.45; dt=1; cprho=4186800;
CC = kair*dx/(D*k);
r=k*dt/(cprho*(dx)^2);

%Define left side tridiagonal matrix for the vertical direction
b=2+2*r;
c=-r;
a=-r;
Acol = b*diag(ones(n,1)) + c*diag(ones(n-1,1),1) + a*diag(ones(n-1,1),-
1);
for i=1:m
    for j=i*n
        Avert(j-(n-1):j,j-(n-1):j)=Acol(:, :);
    end
end

%Define left side tridiagonal matrix for the horizontal direction
%for diagonal c
for i=1:(m-1)
    Q(i,1) = (1+1/(2*(i-.5)));
end
%for diagonal a
for i=1:(m-1)
    Q2(i,1) = (1-1/(2*(i+.5)));
end
b=2+2*r;
```

```

c=-r;
a=-r;
Arow = b*diag(ones(m,1)) + c*diag(Q,1) + a*diag(Q2,-1);
for i=1:n
    for j=i*m
        Ahorz(j-(m-1):j,j-(m-1):j)=Arow(:, :);
    end
end

%Define the number of time steps, where t is in seconds
for t=1:2,
%Define right side matrix for the vertical direction
var u l
Bx = [];
for j=2:(m+1);
    for i=2:(n+1);
        if i<3, u=1, else u=0, end;
        if i>n, l=1, else l=0, end;
Bx(i-1+(j-2)*n, :) = [r*(1-1/(2*(j-1.5)))*T(i,j-1)+(2-
2*r)*T(i,j)+r*(1+1/(2*(j-1.5)))*T(i,j+1)+u*r*T(i-1,j)+l*r*T(i+1,j)];
    end
end

%Multiply the matrices to solve for the new temperatures
Tx = (Avert^-1)*Bx;

%Reorganize the temperature data to fit the original grid
Thalf = [];
Thalf(1,1:(m+2)) = Tj; Thalf(1:(n+2),1) = Ti; Thalf((n+2),1:(m+2)) =
Ti; Thalf(1:(n+2), (m+2)) = Ti;
for p=2:(m+1);
Thalf(2:(n+1),p) = Tx(1+n*(p-2):(p-1)*n,1);
end

%Define right side matrix for the horizontal direction
By = [];
for j=2:(n+1);
    for i=2:(m+1);
        if i<3, u=1, else u=0, end;
        if i>m, l=1, else l=0, end;
By(i-1+(j-2)*m, :) = [r*Thalf(j-1,i)+(2-
2*r)*Thalf(j,i)+r*Thalf(j+1,i)+u*r*(1-1/(2*(i-1.5)))*Thalf(j,i-
1)+l*r*(1+1/(2*(i-1.5)))*Thalf(j,i+1)];
    end
end

%Multiply the matrices to solve for the new temperatures
%Note: These temperatures are considered valid, whereas Thalf is not
Ty = (Ahorz^-1)*By;

%Reorganize the temperature data to fit the original grid
T(1,1:(m+2)) = Tj; T(1:(n+2),1) = Ti; T((n+2),1:(m+2)) = Ti;
T(1:(n+2), (m+2)) = Ti;
for p=2:(n+1);
T(p,2:(m+1)) = Ty(1+m*(p-2):(p-1)*m,1);
end

```

```

%Temperature of the surface of the specimen for each full time step
Tt(t,1:m)=T(2,2:(m+1));

%end time loop
end

```

## **Program 2: Cylindrical Semi-Infinite Solid with Convective Boundary Condition**

```

%Transient heat transfer for semi-infinite solid with an initial
surface temp of Ts,
%with an upper boundary of convective heat transfer where Tj < Ts.
%Load workspace: ADInxmconv.mat
%n =grid dimension representing the number of rows within the boundary
layers
n=12;
%m =grid dimension representing the number of columns within boundary
layers
%Note: m must be an odd integer
m=140;
dx=.00025;
%Define initial grid temperatures
T = [];
%Set initial Skin Temperature
Ts = 28; k=.21; del=.003;
%Define Jet properties
Tjin=16; kair=.026; D=.003; Tair = 19; Tdeep=37;
%Find ambient Nusselt Number
Nufar=((kair*del/(D*k))*((Tdeep-Tair)/(Tdeep-Ts)-1))^(-1);
%Nufar=0;
%Shift Nusselt Numbers
Nu2 = Nu + (Nu(1,1)-Nu)*((Nufar-Nu(61,1))/(Nu(1,1)-Nu(61,1)));
%Fit to dx
Nuint = spline(X,Nu2,.5*dx:dx:.06-.5*dx);
Xint = (.5*dx:dx:.06-.5*dx);
%Jet Temperatures as a function of r
for i=1:(m+2)
Tj(1,i) = Tair*(1-(1-Tjin/Tair)*exp(-500*(i-1)*dx));
end
T(1,:) = Tj;
%Define heat transfer and grid properties
dt=.5; cprho=4186800;
CC = kair*dx/(D*k);
r=k*dt/(cprho*(dx)^2);
%Initial Temps
U = (0:dx:dx*n);
Tinit(1,1:n+1) = ((Tdeep-Ts)/(dx*n))*U+Ts;
for i=1:m+2
T(2:(n+2),i)= Tinit';
end

%Define left side tridiagonal matrix for the vertical direction
b=2+2*r;
c=-r;
a=-r;

```

```

Acol = b*diag(ones(n,1)) + c*diag(ones(n-1,1),1) + a*diag(ones(n-1,1),-
1);
for i=1:m
    for j=i*n
        Avert(j-(n-1):j,j-(n-1):j)=Acol(:, :);
    end
end
for i=1:m
    bt(i,1)= 2+r*(1+Nuint(1,i)*CC)
end
for i=1:m
    Avert(1+n*(i-1),1+n*(i-1))=bt(i,1);
end
%Calculate inverse of matrix
AvertI=inv(Avert);

%Define left side tridiagonal matrix for the horizontal direction
%for diagonal c
for i=1:(m-1)
    Q(i,1) = (1+1/(2*(i-.5)));
end
%for diagonal a
for i=1:(m-1)
    Q2(i,1) = (1-1/(2*(i+.5)));
end
b=2+2*r;
c=-r;
a=-r;
Arow = b*diag(ones(m,1)) + c*diag(Q,1) + a*diag(Q2,-1);
for i=1:n
    for j=i*m
        Ahorz(j-(m-1):j,j-(m-1):j)=Arow(:, :);
    end
end
b=2+r;
c=-.5*r;
a=-.5*r;
Arow1 = b*diag(ones(m,1)) + c*diag(Q,1) + a*diag(Q2,-1);
Ahorz(1:m,1:m) = Arow1;
%Calculate inverse of matrix
AhorzI = inv(Ahorz);

%Define the number of time steps
tf=240;
for t=1:tf,

%Define right side matrix for the vertical direction
var u l
Bx = [];
for j=2:(m+1);
    for i=2:(n+1);
        if i<3, u=1, else u=0, end;
        if i>n, l=1, else l=0, end;
        Bx(i-1+(j-2)*n,:) = [r*(1-1/(2*(j-1.5)))*T(i,j-1)+(2-
2*r)*T(i,j)+r*(1+1/(2*(j-1.5)))*T(i,j+1)+u*r*T(i-1,j)+l*r*T(i+1,j)];];

```

```

Bxtop(i-1+(j-2)*n,:) = u*[r*.5*(1-1/(2*(j-1.5)))*T(i,j-1)+(2-
r)*T(i,j)+r*.5*(1+1/(2*(j-1.5)))*T(i,j+1)+r*Nuint(1,j-1)*CC*T(i-1,j)];
    end
end
Bxf = Bxtop
for i=1:m
    for j=i*n
Bxf(j-(n-2):j,1) = Bx(j-(n-2):j,1);
    end
end
%Multiply the matrices to solve for the new temperatures

Tx = AvertI*Bxf;

%Reorganize the temperature data to fit the original grid
Thalf = [];
Thalf(1,1:(m+2)) = Tj; Thalf(2:(n+2),1) = Tinit'; Thalf((n+2),1:(m+2))
= Tdeep; Thalf(2:(n+2),(m+2)) = Tinit';
for p=2:(m+1);
Thalf(2:(n+1),p) = Tx(1+n*(p-2):(p-1)*n,1);
end

%Define right side matrix for the horizontal direction
By = [];
for j=2:(n+1);
    for i=2:(m+1);
        if i<3, u=1, else u=0, end;
        if i>m, l=1, else l=0, end;
        if j<3, w=1, else w=0, end;
By(i-1+(j-2)*m,:) = [r*Thalf(j-1,i)+(2-
2*r)*Thalf(j,i)+r*Thalf(j+1,i)+u*r*(1-1/(2*(i-1.5)))*Thalf(j,i-
1)+l*r*(1+1/(2*(i-1.5)))*Thalf(j,i+1)];];
Bytop(i-1+(j-2)*m,:) = w*[r*Nuint(1,i-1)*CC*Thalf(j-1,i)+(2-
r*(1+Nuint(1,i-1)*CC))*Thalf(j,i)+r*Thalf(j+1,i)+u*.5*r*(1-1/(2*(i-
1.5)))*Thalf(j,i-1)+l*.5*r*(1+1/(2*(i-1.5)))*Thalf(j,i+1)];];
    end
end

Byf(1:m,1) = Bytop(1:m,:);
Byf(m+1:m*n,1) = By(m+1:m*n,1);

%Multiply the matrices to solve for the new temperatures
%Note: These temperatures are considered valid, whereas Thalf is not
Ty = Ahorzi*Byf;

%Reorganize the temperature data to fit the original grid
T(1,1:(m+2)) = Tj; T(2:(n+2),1) = Tinit'; T((n+2),1:(m+2)) = Tdeep;
T(2:(n+2),(m+2)) = Tinit';
for p=2:(m+1);
T(p,2:(m+1)) = Ty(1+m*(p-2):(p-1)*m,1);
end

%Temperature of the surface of the specimen for each full time step
clear tt Tv Tview

```

```

tt(:,1)= [0:2*dt:2*tf*dt];
Tt(1:tf+1,1) = tt(:,:);
Tt(1,2:m+1)=[Ts:Ts];
Tt(t+1,2:m+1)=T(2,2:(m+1));

%end time loop
end

%Elliptical view correction
for i = 1:(tf+1)
Tav1(i,:) = Tt(i,2)/((17^2)*(sqrt(2)));
end
for i = 1:(tf+1)
    for j = 2:17
        Tav2(i,j-1) = (Tt(i,j+1)*(j-.5))*2/((17^2)*sqrt(2));
    end
end
Tav2 = sum(Tav2,2);

for i = 1:(tf+1)
    for j = 18:24
        Tav3(i,j-17) = Tt(i,j+1)*(j-.5)*atan(sqrt((2-((j-.5)/17)^2)/(2*((j-.5)/17)^2-2))*.6366*2/((17^2)*sqrt(2));
    end
end
Tav3 = sum(Tav3,2);

for i = 1:(tf+1)
    Tav(i,2)=Tav1(i,1)+Tav2(i,1)+Tav3(i,1);
end
Tav(1:t+1,1) = tt(:,:);

```

## References

- [1] American Burn Association. "Burn Incidence and Treatment in the US Fact Sheet: 2007." American Burn Association. Aug 5, 2008. <[http://www.ameriburn.org/resources\\_factsheet.php](http://www.ameriburn.org/resources_factsheet.php)>.
- [2] Christopher J. Wieczorek and Nicholas A. Dembsey. "Human Variability Correction Factors for Use with Simplified Engineering Tools for Predictiong Pain and Second Degree Skin Burns." *Journal of Fire Protection Engineering*, Vol. 2. May 2001.
- [3] E. Y-K Ng and L. T. Chua. "Prediction of skin burn injury. Part 1: numerical modelling." *Proc Instn Mech Engrs*, Vol 216 Part H.
- [4] E. Y-K Ng and L. T. Chua. "Prediction of skin burn injury. Part 2: parametric and sensitivity analysis." *Proc Instn Mech Engrs*, Vol 216 Part H.
- [5] Fred M. Dickey, Scott C. Holswade, and Mark L. Yee. "Burn Depth Estimation Using Thermal Excitation and Imaging." Part of the SPIE Conference on Biomedical Diagnostic, Guidance, and Surgical-Assist Systems. San Jose, California, January, 1999.
- [6] Andrew Hargroder, James Davidson, Donald Luther, and Jonathan Head. "Infrared imaging of burn wounds to determine burn depth." Part of the SPIE Conference on Infrared Technology and Applications XXV, Orlando, Florida, April 1999.
- [7] Shunichi Sato, et al. "Measurement of photoacoustic signals from skin: Potential application to burn depth estimation." *Hybrid and Novel Imaging and New Optical Instrumentation for Biomedical Applications*, Proceedings of SPIE Vol. 4434 (2001).
- [8] Frank P. Incropera and David DeWitt. Fundamentals of Heat and Mass Transfer. John Wiley & Sons, Inc. 2002.
- [9] H. Martin. "Heat and Mass Transfer between Impinging Gas Jets and Solid Surfaces," in J. P. Hartnett and T. F. Irvine, Jr., Eds., *Advances in Heat Transfer*, Vol 13, Academic Press, New York, 1977.
- [10] Kevin Spangler. "Energy Transport in Fire Fighter Protective Clothing." University of Maryland, College Park. 2008.
- [11] Lorenzo Leonardi, et al. "A Near Infrared Spectroscopic Approach to Assess Tissue Viability Following a Thermal Injury." *Biomarkers and Biological Spectral Imaging*, Proceedings of SPIE Vol 4259 (2001).
- [12] Xiqin Zhang, and Da Xing. "Determination of simulated burn depth using relative fluctuation of backscattering light." *Biomedical Photonics and Optoelectronic Imaging*, Proceedings of SPIE Vol. 4224 (2000).

- [13] S. Elton, and R. Staples. "The Use of Modelling in Burn Injury Evaluation Beneath Clothing Layer." *Fire and Materials*, vol 23, 1999.
- [14] Harry H. Pennes. "Analysis of Tissue and Arterial Blood Temperatures in the Resting Human Forearm." *Journal of Applied Physiology*, Vol 1. Aug 1948.
- [15] Konrad Buettner. "Effects of Extreme Heat and Cold on Human Skin. I. Analysis of Temperature Changes Caused by Different Kinds of Heat Application." *Journal of Applied Physiology*, Vol 3, June 1951.
- [16] Alice M. Stoll. "Heat Transfer in Biotechnology." Aerospace Medical Research Department U.S. Naval Air Development Center Johnsville, Warminster, Pennsylvania.
- [17] John A. Weaver, and Alice Stoll. "Mathematical Model of Skin Exposed to Termal Radiation." *Aerospace Medicine*. January 1969.
- [18] D. C. Ross, and K. R. Diller. "An Experimental Investigation of Burn Injury in Living Tissue." *Journal of Heat Transfer*. May, 1976.
- [19] Kenneth R. Diller. "Analysis of Skin Burns." Department of Mechanical Engineering, Biomedical Engineering Center, University of Texas, Austin, Texas.
- [20] Kenneth R. Diller, and Linda J. Hayes. "Analysis of tissue injury by burning: comparison of *in situ* and skin flap models." *Int. J. Heat Mass Transfer*. Vol 34, No. 6, pp. 1393-1406, 1991.
- [21] John Halin, et al. "A Sensitivity Study of a Variable-Property Skin Burn Model Considering the Variability of Water Content." *Performance of Protective Clothing: Fifth Volume*, ASTM STP 1237, American Society for Testing and Materials, 1996.
- [22] National Fire Protection Association. The SFPE Handbook of Fire Protection Engineering. 2002.
- [23] Steven C. Chapra, and Raymond P. Canale. Numerical Methods for Engineers: Second Edition. McGraw-Hill Book Company, 1988.
- [24] David C. Lay. Linear Algebra and Its Applications: Third Edition. Pearson Education, Inc. 2006.